ACS APPLIED MATERIALS & INTERFACES

Research Article

www.acsami.org

Constructing a High-Efficiency MoO_3/Polyimide Hybrid Photocatalyst Based on Strong Interfacial Interaction

Chenghai Ma,[†,‡] Jun Zhou,[†] Haoyue Zhu,[§] Weiwei Yang,[†] Jianguo Liu,[†] Ying Wang,*[,†] and Zhigang Zou*[,†]

[†]Eco-materials and Renewable Energy Research Center (ERERC), School of Chemistry and Chemical Engineering, National Laboratory of Solid State Microstructures, Kunshan Innovation Institute of Nanjing University, Jiangsu Key Laboratory for Nanotechnology, Nanjing 210093, People's Republic of China

[‡]School of Chemical Engineering, Qinghai University, Qinghai 810016, China

[§]Department of Chemistry, The Pennsylvania State University, University Park, Pennsylvania 16802, United States

Supporting Information

ABSTRACT: A novel two-dimensional hybrid polymer photocatalyst black-MoO_3/polyimide was synthesized by one-pot thermopolymerization of monomers, ammonium molybdate, and thiourea at mild temperatures. Thiourea and ammonium molybdate as fluxing agents promote the formation of black molybdenum oxide (BMO) on polyimide (PI) and enhance the crystallinity of PI. It is confirmed by X-ray photoelectron spectroscopy, electron paramagnetic resonance, and Fourier transform infrared that the strong interaction between BMO and PI leads to the formation of a Mo−N coordination bond through the coordination of N atoms of heptazine units to the unsaturated Mo atoms of BMO and results in a large number of Mo^{5+} cations in BMO/PI. UV−vis and photoluminescence reveal that the visible light absorption of BMO/PI was increased and the separation efficiency of photogenerated electron/hole obviously was significantly enhanced, which facilitates the improvement of the photocatalytic activity of BMO/PI. This work provides a new approach to synthesizing efficient inorganic−organic hybrid semiconductor photocatalysts.

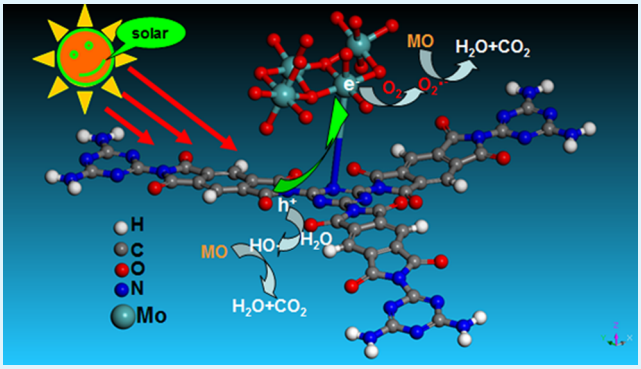

KEYWORDS: *polyimide, hybrid photocatalyst, molybdenum trioxide, visible light irradiation, degradation*

1. INTRODUCTION

Serious energy shortage and environment pollution are becoming worldwide intractable problems. One of the best ways to settle these problems is to develop high-efficiency photocatalysts for utilizing renewable solar energy to efficiently degrade pollutants. Besides the traditional transition metal oxide semiconductors,[1−3] polymer photocatalysts have attracted much attention in recent years because of their abundant sources, low cost, unique chemical stability, and tunable structures. These metal-free semiconductors were reported to be promising photocatalytic materials for water-splitting hydrogen generation and organic pollutant degradation under visible light.[4−7] However, the inherent feature of the carrier's transition and photonic excitation of conjugated polymer limit their photocatalytic efficiency.[8] Thereafter, many efforts have been made to narrow the bandgap and improve carrier transport of polymer semiconductors by loading co-catalysts to enhance their photocatalytic performance.[9−12] These investigations shed some light on utilizing innovative hybrid polymer photocatalyts. Polyimides (PIs), one kind of conjugated polymers, have been widely reported for their synthesis and applications as absorbents or chemosensors.[13−16] However, to the best of our knowledge, no investigations of the photocatalytic property of polyimide have been reported. Very recently, our group reported a novel green approach to synthesizing a polyimide (PI) photocatalyst. The synthesis was conducted at 200 °C, which is lower than that of graphitic carbon nitrides (g-C_3N_4), and the synthesis does not give off ammonia.[17,18] Although possessing high activity of hydrogen generation from water splitting and pollutant degradation, the polymer photocatalyst has a relatively wide bandgap (2.7 eV), which is expected to be narrowed for efficiently utilizing solar energy. In general, narrowing the bandgap of the semiconductor can be realized by lowering the conduction band or elevating the valence band. However, both strategies weaken the reducing power of photoinduced electrons and the oxidizing power of photoinduced holes, which probably lead to the noncontribution of photonic

Received: February 11, 2015
Accepted: June 25, 2015
Published: June 25, 2015

DOI: 10.1021/acsami.5b01356
ACS Appl. Mater. Interfaces 2015, 7, 14628−14637

excitation for the target reaction. Moreover, elevating the energy level of the valence band may result in a structural instability of the polymer photocatalyst because its original energy level of the highest occupied molecular orbital (HOMO) is usually high. Therefore, an elaborative balance to the photonic energy and optical absorption region for visible light depends on good band matching between the polymer and the co-catalyst. More significantly, deeper insight into the intrinsic interaction between the interface of the co-catalyst and polymer is very necessary for designing a high-efficiency hybrid polymer photocatalyst.

Molybdenum(VI) oxide (MoO_3) is considered to be a promising candidate for the modification of the band structure of the PI photocatalyst because of its unique energetic and electrical properties.[19−22] Although molybdenum(VI) oxide (MoO_3) has many applications in various organic electronic devices,[23,24] no studies of PI coupled with MoO_3 as the energy band modifier of a polymer photocatalyst have been reported to the best of our knowledge. Herein, we report a novel inorganic−polymer hybrid photocatalyst (BMO/PI) synthesized by a one-pot thermal polymerization method. The resulting composites show enhanced visible light photocatalytic activity compared to that of pristine PI. The textural, electronic, and optical properties of the obtained hybrid materials are carefully characterized by various spectral techniques. The effect of the MoO_3 content of samples on the degradation efficiency of methyl orange (MO) under visible light irradiation was discussed in detail, and a possible photocatalytic mechanism was also proposed.

2. EXPERIMENTAL METHODS

2.1. Synthesis of the Photocatalyst. Melamine (MA) and pyromellitic dianhydride (PMDA) were purchased from Tokyo Chemical Industry Co., Ltd., and SCR Sinopharm Chemical Reagent Co., Ltd., respectively, while hexaammonium heptamolybdate tetrahydrate $[(NH_4)_6Mo_7O_{24}\cdot 4H_2O]$ and thiourea were purchased from Nanjing Chemical Reagent Co., Ltd. All chemicals were used without further purification. For the synthesis of 1 g of 0.5BMO/PI, the procedure is typically as follows: 0.386 g of MA, 0.666 g of PMDA, 0.006 g of $[(NH_4)_6Mo_7O_{24}\cdot 4H_2O]$, and 0.007 g of thiourea were mixed uniformly in an agate mortar. The mixture was put into a loosely covered porcelain crucible and then heated at a rate of 7 °C min^{-1} to 325 °C and kept at this temperature for 4 h prior to being cooled. The resulting solid was collected and ground into a powder. The chemical reaction for the preparation of the samples is as follows:

$$C_3H_6N_6 + C_{10}H_2O_6 + (NH_4)_6Mo_7O_{24}\cdot 4H_2O + CS(NH_2)_2 \xrightarrow{325\ ^\circ C(4\ h)} (C_{21}H_3O_6N_9)_n\cdot MoO_{3-x} + NH_3 + SO_2 + CO_2 + NO_2 + H_2O$$

To remove the residual unreacted MA monomer completely, the powder was washed with 50 °C distilled water several times, followed by filtration and drying at 80 °C for 6 h. Then a yellowish sample was obtained and denoted as 0.5BMO/PI. In the same way, a series of *x*BMO/PI samples were prepared by a similar method, where *x* represents the weight percent of MoO_3 in the sample. For comparison, pristine MoO_3, BMO, 3.0MoO_3/PI, 3.0S/PI, and PI were prepared according to the same process. The amounts of reactants for synthesis of the samples are summarized in Table S1 of the Supporting Information.

The structural analysis, including elemental analysis, solid-state ^{13}C nuclear magnetic resonance, etc., has confirmed the structural composition and framework of the polymer chain of PI in our previous work.[18]

2.2. Characterization. Powder X-ray diffraction (PXRD) patterns of the samples were recorded on a Rigaku diffractometer using Cu Kα radiation in the 2θ range from 5 to 70, and the X-ray tube was operated at 40 kV and 40 mA. Fourier transform infrared (FTIR) measurements were taken on a Nicolet NEXUS870 spectrometer using the KBr pellet support. The scanning electron microscope (SEM) image was recorded on a Hitachi S4800 FE-SEM system. The transmission electron microscope (TEM) image was obtained on a JEM-2100 electron microscope. UV−vis diffuse reflection spectroscopy (DRS) was performed on a Shimadzu UV-3600 spectrometer using $BaSO_4$ as the reference. The photoluminescence (PL) spectrum was recorded with a Varian Cary eclipse spectrometer with an excitation wavelength of 350 nm at room temperature. X-ray photoelectron spectroscopy (XPS) and valence band X-ray photoelectron spectroscopy (VBXPS) were conducted using a PHI 5000 Versa Probe X-ray photoelectron spectrometer with monochromatized Al Ka X-ray radiation. Electron paramagnetic resonance (EPR) measurement was conducted on a Bruker EMX-10/12 EPR spectrometer at room temperature.

2.3. Electrochemical Analysis. The working electrode was prepared on a fluorine-doped tin oxide (FTO) transparent conductive film glass; 50 mg of powder was mixed with 2 mL of acetone under sonication for 30 min to obtain a slurry. The slurry was spread onto FTO glass whose side part was previously protected using Scotch tape. After being air-dried, the electrode was heated at 260 °C for 30 min in air to improve adhesion. Electrochemical measurements were performed in a typical three-electrode cell, using a Pt sheet and a Ag/AgCl electrode as the counter electrode and reference electrode, respectively. The electrochemical experiments were conducted on an electrochemical analyzer (CHI-663C, Shanghai Chenhua, China). The working electrode was immersed in a 0.5 mol L^{-1} Na_2SO_4 (pH 6.8) electrolyte solution and irradiated from the back side (FTO substrate/semiconductor interface) to minimize the influence of the thickness of the semiconductor layer. The exposed area under illumination was 0.28 cm^2. For Nyquist plot measurements, the perturbation signal was 10 mV and the frequency ranged from 200 kHz to 10 mHz.

2.4. Photocatalytic Test. The photocatalytic activity of the samples for methyl orange (MO) degradation was measured in a Pyrex top-irradiation vessel. The temperature of the reactor was held at 25 °C by a constant-temperature water system. Typically, 0.2 g of catalyst was dispersed in a 100 mL aqueous solution of MO (4 mg L^{-1}). To establish an adsorption equilibrium, the suspension was magnetically stirred in the dark for 1 h prior to irradiation under a xenon 300 W lamp equipped with a cutoff filter (λ > 420 nm; I = 20 A) and a cooling fan. At the given irradiation time intervals, a reaction mixture (3−4 mL) was withdrawn and centrifuged to remove the catalyst particles. Then the obtained clear solution was analyzed by measuring its absorbance at 464 nm with a UV−vis spectrometer (Shimadzu UV-1750). To further evaluate the stability of the photocatalyst, cycle experiments were conducted for four runs, and the irradiation time of each run was 10 h. The used sample could be conveniently separated and collected from the solution by high-speed centrifugation and added back into the reactor for the next cycle.

3. RESULTS AND DISCUSSION

3.1. Structure and Morphology Analysis. Figure 1 illustrates the XRD patterns of pristine PI and BMO/PI composites with different MoO_3 contents. Several distinct peaks in the range of 10−30° appeared on the pattern of pristine PI, indicating that the two monomers of MA and PMDA have polymerized into the framework of PI.[18] These characteristic peaks of PI can be clearly observed on the patterns of BMO/PI, which confirms that incorporation MoO_3 into PI did not change the original crystal structure and polymeric chain of PI. Intriguingly, no diffraction peaks relevant to any Mo species can be observed on the patterns of BMO/PI samples, mirroring a high level of dispersion of Mo species on PI photocatalysts. We speculate that the absence of the

DOI: 10.1021/acsami.5b01356
ACS Appl. Mater. Interfaces 2015, 7, 14628−14637

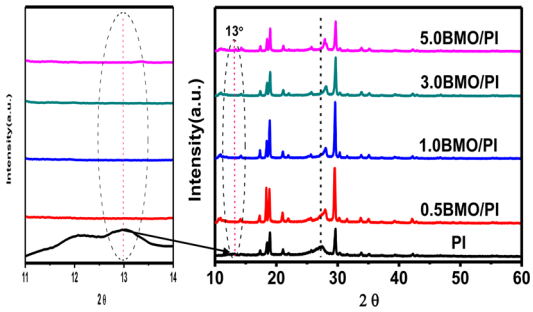

Figure 1. XRD patterns of PI and BMO/PI.

characteristic peaks of MoO_3 in XRD patterns of BMO/PI is probably due to the very small amount of MoO_3 and stronger guest–host interaction that will be verified later by FTIR. The existence of hidden structural features of the loaded transition metal oxide Fe_2O_3 on polymer photocatalyt g-C_3N_4 was also reported,[25] and the characteristic diffraction peaks of the iron species were absent even when iron contents were as high as 20 wt % in g-C_3N_4, which was ascribed to the strong chemical coordination of the iron species to the g-C_3N_4 host. It is worth noting that the loading of BMO onto PI does not change the peak features of PI, while the intensities of the characteristic peaks were greatly improved. Additionally, the XRD peak centered at 27.4° shifted slightly to the high angle of 28.0° after the introduction of the Mo component, corresponding to a decrease from 3.25 to 3.18 Å in the interlayer stacking of the conjugated aromatic system of PI.[4] This compact stacking of π-conjugated two-dimensional (2D) frameworks of the polymer is expected to improve the stability of BMO/PI photocatalysts. Curiously, the very weak diffraction peak located at ~13° in the XRD pattern of PI disappears after BMO is loaded into PI. According to the previous work,[4] the small peak at 13° in the XRD patterns of the 2D conjugated polymer is attributed to an in-plane repeat period of 0.681 nm in the crystal. The small peak located at ~13° in the XRD spectra of BMO/PI samples is missing, presumably because of the strong interaction between BMO and PI, which probably leads to a coordination Mo–N bond through coordination of N atoms of heptazine units to the unsaturated Mo sites of α-MoO_3 in the interface of BMO/PI (confirmed later by FTIR, XPS, and EPR), thus impacting the formation of an in-plane repeat period of 0.681 nm in the crystal during the synthesis of BMO/PI hybrid photocatalysts. In addition, it is obvious that the peak intensities of all the BMO/PI samples become stronger than that of pristine PI and reached their highest values as the MoO_3 content increases to 1.0 wt %. Above this MoO_3 content, the intensities of peaks begin to decrease for the 3.0BMO/PI sample in which excessive $(NH_4)_6Mo_7O_{24}\cdot 4H_2O$ and thiourea were added as reactants. To determine the reasons for the improved crystallinity of BMO/PI, we prepared 3.0MoO_3/PI and 3.0S/PI samples as contrast examples without adding thiourea and $(NH_4)_6Mo_7O_{24}\cdot 4H_2O$ to the reactant system, respectively. As shown in Figure S1 of the Supporting Information, the XRD peak intensities of 3.0MoO_3/PI and 3.0S/PI are comparable to that of PI while the peak of 3.0BMO/PI is significantly enhanced. These results imply that the thiourea in the synthesis of PI only acts as a molten flux to homogenize the reactant system and facilitate the polymerization of the two monomers, whereas the role of $(NH_4)_6Mo_7O_{24}\cdot 4H_2O$ is as the acidic oxide catalyst of the polymerization reaction after the decomposition. Therefore, the crystallinitiy of the BMO/PI photocatalyst can be significantly improved only when $(NH_4)_6Mo_7O_{24}\cdot 4H_2O$ and thiourea are simultaneously added to the reactant system. It may be attributed to the special thermal polymerization approach of PI in which PMDA molecules first reach a molten state and react with adjacent MA molecules to form oligomeric polyimides,[14] and then these oligomers further polymerize with the aid of the hydrogen-bonding or π–π electronic interaction between the conjugated core units, leading to the assembly of highly symmetrical and regular polymer frameworks.[26] With the addition of $(NH_4)_6Mo_7O_{24}\cdot 4H_2O$ and thiourea, the BMO/PI reaction system becomes more uniform because thiourea acts as the molten flux to facilitate the polymerization of the two monomers. On the other hand, MoO_3 generated from the decomposition of $(NH_4)_6Mo_7O_{24}\cdot 4H_2O$ at 190 °C as a Lewis acid catalyst of polymerization further completes the polymerization of MA and PMDA because imidization is generally accelerated under acidic conditions.[27]

The SEM image (Figure 2a) illustrates the layered morphology of 3BMO/PI, indicating a compact arrangement

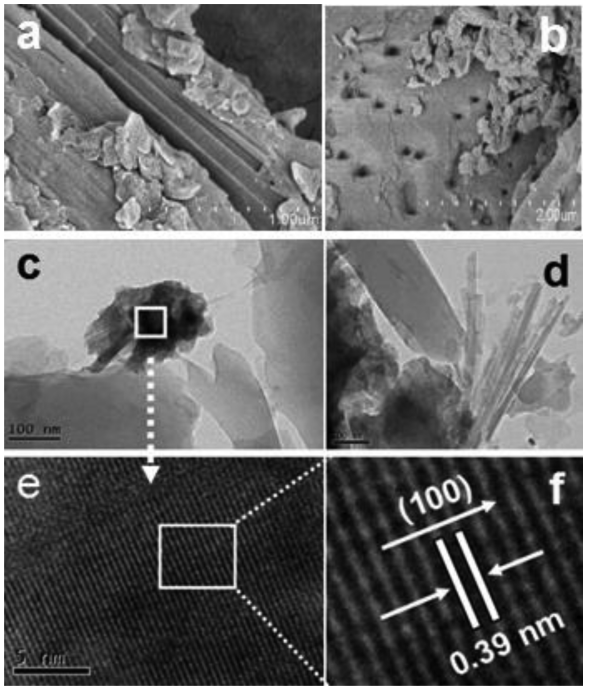

Figure 2. SEM (a and b) and HR-TEM (c–f) images of 3.0BMO/PI.

of nanoplates with a thickness of 20 nm. Some irregular pores can be observed on the surface of the plates (Figure 2b). HR-TEM images clearly demonstrate that the layered plate of BMO/PI consists of some thinner sheets and nanorods (Figure 2c,d). This obvious change from the dendritic branch morphology of PI (Figure S2a,b of the Supporting Information) to an ordered lamellar morphology implies a different reaction mechanism after the introduction of MoO_3 onto PI. Being different from that for the synthesis of PI, the reactant mixture for the synthesis of BMO/PI contains both molybdate and thiourea. Molten salt $(NH_4)_6Mo_7O_{24}\cdot 4H_2O$ and thiourea can act as good solvents to promote the further polymerization of the dendrite and its growth in the 2D direction, which is similar to the "ionothermal route" for the synthesis of ordered 2D polymer covalent frameworks based on heptazine units.[28] The decomposition of thiourea functions as a pore-making agent in the synthesis process, resulting in some of

DOI: 10.1021/acsami.5b01356
ACS Appl. Mater. Interfaces 2015, 7, 14628–14637

the pores on the surface of the BMO/PI sample. Noticeably, the clear lattice stripes with a distance of 0.39 nm between the stripes (Figure 2e,f) reveal that the layered MoO_3 nanocrystal is in a perfect (100) plane orientation on PI. Energy dispersive spectroscopy (EDS) further corroborates that the nanosheets on the surface of PI are rich in Mo and N elements (Figure S3 of the Supporting Information). To pursue the predominate (100) orientation of MoO_3, we prepared two MoO_3 samples by sintering net $(NH_4)_6Mo_7O_{24}\cdot 4H_2O$ and the mixture of $(NH_4)_6Mo_7O_{24}\cdot 4H_2O$ and thiourea (named BMO) at 325 °C for 4 h under an ambient atmosphere. It was found that only α-MoO_3 was obtained by both methods (Figure S4a of the Supporting Information). Several main characteristic diffraction peaks at 2θ angles of 12.8, 23.5, 25.7, 27.4, 33.9, 39.0, 46.2, and 49.4°, corresponding to (020), (110), (040), (021), (111), (060), (210), and (002) diffraction lines, respectively, can be indexed to the orthorhombic α-MoO_3 (JCPDF Card 05-0508) and match well with previous reports.[29,30] However, two samples exhibit highly anisotropic growth of the α-MoO_3 crystals. The sample BMO obtained from heating the mixture of $(NH_4)_6Mo_7O_{24}\cdot 4H_2O$ and thiourea demonstrates a preferential growth along (110) and (021) faces, while the MoO_3 crystal obtained by sintering net $(NH_4)_6Mo_7O_{24}\cdot 4H_2O$ shows an apparent increase in the intensity of (0k0) faces. More surprisingly, the BMO sample is a black color, while the latter MoO_3 sample was a yellow powder (Figure S4b of the Supporting Information). Lee et al. had reported that the color of the MoO_3 film changed from pale yellowish to black after it had been annealed at 300 °C under high vacuum (10^{-6} Torr). This color change was ascribed to the formation of oxygen vacancies in vacuum.[31] It is probably the decomposition of the coexisting thiourea in the synthesis of BMO/PI that consumes a large amount of oxygen and results in an oxygen deficient reaction condition, leading to the formation of large quantities of oxygen vacancies and thus black molybdate oxide (BMO) on PI. To further confirm the existence of oxygen vacancies on BMO, the EPR measurements of BMO and MoO_3 were performed under the same condition (at room temperature). As shown in Figure S5a of the Supporting Information, the very strong signals of paramagnetic oxygen vacancies $V_O^\bullet$ (surface $V_O^\bullet$ signal at 3434 G; lattice $V_O^\bullet$ signal at 3479 G)[32] and Mo^{5+} ion ($4d^1$) ($g_\perp = 1.932$, and $g_\parallel = 1.895$)[33] can be easily observed in the spectra of the BMO sample, but the signals of paramagnetic oxygen vacancies $V_O^\bullet$ in the spectrum of the pristine MoO_3 sample are nearly negligible at room temperature. These oxygen vacancies $V_O^\bullet$ on BMO arise from the lattice oxygen escaping when MoO_3 is heated under hypoxic conditions, where Mo^{6+} must be reduced to Mo^{5+} to maintain charge neutrality; thus, the empty $4d^0$ band of MoO_3 becomes partially occupied with electrons.[19,34] Therefore, the color of the sample from PI to 5.0BMO/PI becomes darker as the Mo content increases (Figure S5b of the Supporting Information). HR-TEM imagines illustrate that the morphologies of two samples are very different: BMO exhibits a closely packed one-dimensional (1D) nanorod structure, but the MoO_3 sample possesses an irregular blocky structure (Figure S4c of the Supporting Information). These results reveal that the eutectic decomposition of $(NH_4)_6Mo_7O_{24}\cdot 4H_2O$ with thiourea can change the morphology of the resulting α-MoO_3 and improve its structural ordering. Song et al. also found that the surface morphology of the obtained α-MoO_3 nanocrystals could transform from three-dimensional particles through a 1D nanobelt to 2D multilayer when the oxidizing temperature of MoO_2 was increased, and the 2D multilayers α-MoO_3 crystals with the perfect (100) plane only could be obtained at a high temperature of 700 °C.[29] Intriguingly, this study indicates that the α-MoO_3 crystals with the perfect (100) orientation can be formed on PI at a rather low temperature of 325 °C. It is probably attributed to the strong structural induction effect of layered PI during the growth process of α-MoO_3 crystals. As we previously reported, polyimidization of PI is a typical melt-annealing synthetic process, in which two monomers of MA and PMDA first melt at low temperatures and then react to form amorphous oligomeric polyimide at ~250 °C, and these oligomers further coalesce to generate the lamellar structure of PI as the temperature increases to 325 °C.[18,35] In the synthesis of hybrid composite BMO/PI, eutectic melting of the two monomers, $(NH_4)_6Mo_7O_{24}\cdot 4H_2O$ and thiourea, occurs at a temperature lower than the polymerization temperature of PI. As the temperature increases to 250 °C, the in situ-generated oligomeric polyimide probably forms "molecule−ion aggregates".[29] Then the further polycondensation of the oligomers at a higher temperature produces the large conjugated frameworks of the lamellar structural polymer that can play a role as the template for the predominate (100) orientation of α-MoO_3 crystals in the interface PI. Such a predominate (100) orientation of α-MoO_3 is related to the interface interaction between α-MoO_3 and PI. We have reported that the electronic charge distribution on the 2D framework of PI is nonuniform and the role of MA moieties as electron donors.[17,18,26] This nonuniform distribution of electronic charge may affect the orientation of α-MoO_3 on PI depending on the electronic interaction. As we know that there are some bare Mo sites at the (100) face of MoO_3,[36] these electronically positive Mo sites tend to interact with the electrostatic potential matching sites of PI and lead to the predominate (100) orientation of the layered α-MoO_3 nanocrystals.

The interface interaction of BMO/PI is verified by FTIR spectroscopy (Figure 3). In the FTIR spectrum, all the samples

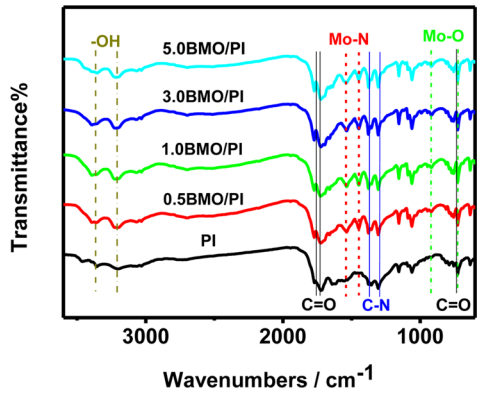

Figure 3. FTIR spectrum of PI and BMO/PI.

display the characteristic absorption bands of polyimide, which have been reported in previous work.[37,38] The bands at 1770.8, 1722.3, and 726.6 cm^{-1} are assigned to the asymmetric stretching, symmetric stretching, and bending vibrations of the imide carbonyl groups, respectively. The bands at 1375 and 1306 cm^{-1} are attributed to the C−N−C stretching vibration in the five-membered imide ring and breathing modes of aromatic CN in the triazine unit, respectively.[26] All these characteristic bands of PI show enhanced intensities in BMO/PI versus those in pristine PI, which easily matches the results of XRD. This

DOI: 10.1021/acsami.5b01356
ACS Appl. Mater. Interfaces 2015, 7, 14628−14637

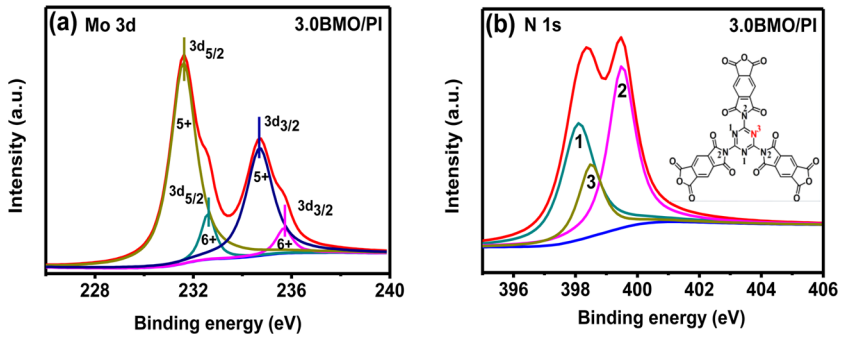

Figure 4. XPS spectra of PI and 3.0BMO/PI composite sample: (a) Mo 3d and (b) N 1s of 3.0BMO/PI composite.

reveals that loading with BMO does not change the framework of PI or its core chemical skeleton but improves the degree of polymerization. More noticeably, the characteristic peaks of the Mo−N bond at 1531 and 1446 cm^{-1} and the Mo−O bond[39] at 908 and 721 cm^{-1} could be clearly observed in the FTIR spectra of BMO/PI, confirming the strong chemical interaction between Mo species and PI. Such strong interaction probably leads to a Mo−N coordination bond through coordination of the N atoms of heptazine units to the unsaturated Mo sites of α-MoO_3 in the interface of BMO/PI. Additionally, the two peaks in the range of 3200−3400 cm^{-1} become stronger and wider, which indicates that there are a number of hydroxyl groups on the surface of BMO/PI. This is because there are many different oxygen sites on the (100) surface of MoO_3, which could bind to hydrogen and result in the local surface OH groups.[36]

The chemical states of Mo and N in the BMO/PI sample were further probed by using high-resolution XPS (Figure 4). The binding energies of all the elements were also referenced to the C 1s peak (284.6 eV) arising from adventitious carbon. For comparison, the spectra of MoO_3 and the BMO were also acquired and are shown in Figure S6a of the Supporting Information. The spectrum of the MoO_3 sample (bottom line) shows only a pair of peaks of Mo $3d_{5/2}$ (232.6 eV) and Mo $3d_{3/2}$ (235.7 eV), originating from the Mo^{6+} cations in the MoO_3 lattice,[40,41] while the spectrum of BMO (top line) displays two additional weak peaks at ~232.1 eV ($3d_{5/2}$) and ~229.8 eV ($3d_{5/2}$) except for the peaks of Mo^{6+} cations; the two new peaks can be attributed to the Mo^{5+} and Mo^{4+}, respectively, associated with the oxygen vacancies.[19,31] In addition, an intensity drop in the O 1s XPS spectra of BMO compared to that of pristine MoO_3 (Figure S6b of the Supporting Information) further consolidates the loss of oxygen in the BMO sample upon thermal decomposition. To our surprise, compared to that of BMO, the intensity of the two peaks assigned to Mo^{6+} dramatically decreases in that of the 3.0BMO/PI hybrid composite (Figure 4), emerging as two small shoulder peaks at binding energies of 232.6 eV ($3d_{5/2}$) and 235.7 eV ($3d_{3/2}$), respectively. The peak assigned to Mo^{4+} at a low binding energy (BE) of 229.8 eV disappears, and concomitantly, the intensities of the two peaks at 231.6 and 234.7 eV assigned to the Mo $3d_{5/2}$ and Mo $3d_{3/2}$ orbital spin splitting of Mo^{5+} sharply increase (Figure 4a). These results clearly indicate that the incorporation of BMO onto PI leads to the transformation of Mo^{6+} to Mo^{5+} species, which indicates that Mo ions are located in an electron-rich environment provided by the N atoms of triazine rings of PI. To ascertain whether the formation of a large number of Mo^{5+} ions resulted from the reduction of thiourea, we conducted comparative experiments without addition of thiourea to the reactants to synthesize sample 3.0MoO_3/PI. It is interesting to note an apparent peak contrast related to a great number of Mo^{5+} ions and a small quantity of Mo^{6+} in the spectrum of the 3.0MoO_3/PI composite (Figure S7a of the Supporting Information), which confirms that the reduction of thiourea is not the reason for the formation of Mo^{5+}. Based on the FTIR results for the formation of the Mo−N bond in 3.0BMO/PI (Figure 3), we suggest that a large number of Mo^{5+} ions may stem from a strong coordination of N to Mo in BMO/PI composites. The change of the chemical environment of N in 3.0BMO/PI has also been studied by comparing the N 1s XPS spectra of pristine PI and 3.0BMO/PI. The peak centered at ~398.1 eV in the spectrum of pristine PI (Figure S7b of the Supporting Information) corresponds to the nitrogen atoms (at position 1) in the heterocycle, and the peak at ~399.4 eV corresponds to the nitrogen atoms in the imide (at position 2). It can be seen in the spectrum of the 3.0BMO/PI composite (Figure 4b) that the relative area of the first peak becomes smaller, implying that the amount of this kind of nitrogen atom in the heterocycle decreases. Neither the position nor the relative area of the second peak changes, indicating that nitrogen atoms of imide are not influenced. Notably, a new kind of N 1s peak centered at ~398.5 eV appears as shown in Figure 4b, mirroring the fact that some nitrogen atoms are located in a changed chemical environment in the structure of the BMO/PI composite. As we know, the formation of the N−Mo bond will increase the binding energy of nitrogen because the electronic density around the N atomic nucleus will decrease when lone pair electrons are provided to molybdenum. Consequently, the new N 1s peak is attributed to nitrogen atoms at position 3 in the structure of the BMO/PI composite. Therefore, this interaction provides an interface electronic charge transfer from polyimide to BMO, which facilitates the photogenerated electron/hole pair dissociation. A similar phenomenon has been found on transition metal oxide-modified C_3N_4 hybrid materials.[12,25,42] As for the absence of the peak related to Mo^{4+} (Figure S7 of the Supporting Information) in that of BMO/PI, it is probably related to the generation of a large amount of Mo^{5+} and a decrease in the amount of Mo^{6+}. Interestingly, the incorporation of BMO into PI also alters the EPR spectra of the PI polymer photocatalyst. As shown in Figure 5, after the incorporation of BMO into PI, the surface oxygen vacancy signal of $V_O^{\bullet}$ at 3434 G disappears on the spectrum of BMO/PI and concomitantly the signal intensity at 3479 G (g = 2.003) becomes significantly stronger than that of PI. The g value equivalent to 2.003 is assigned to an unpaired electron on the carbon atoms of the aromatic rings within π-bonded nanosized clusters.[43] Based on the results of XPS in which the amount of

DOI: 10.1021/acsami.5b01356
ACS Appl. Mater. Interfaces 2015, 7, 14628−14637

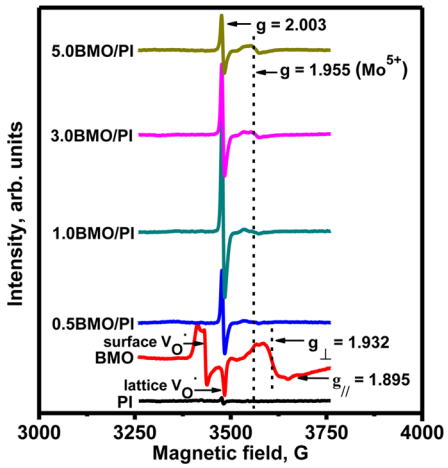

Figure 5. EPR spectra of PI, BMO and BMO/PI samples at room temperature.

Mo^{5+} dramatically increased as the amount of Mo^{6+} decreased, we speculate that the strong coordination of the lone pair electron of N atoms in heptazine units to the unsaturated Mo atoms of BMO results in an increase in the density of the delocalized electrons between BMO and PI. Correspondingly, the intensity of the Lorentzian line with a g value of 2.003 obviously increases with an increasing concentration of BMO in BMO/PI samples and reaches a maximal value at 1.0 wt %, decreasing thereafter. This phenomenon agrees with the change in XRD peak intensity from PI to 5.0BMO/PI (Figure 1). Additionally, it can be seen that the signal intensity of the broad peak at 3566 G (g = 1.955), assigned to the resonance line of Mo^{5+} cations,[44] becomes stronger and shifts from 3607 G (g = 1.932) to 3566 G (g = 1.955) as the BMO content increases, suggesting that N as the electron donor coordinated to Mo makes Mo $4d^1$ orbits tending to be half-full state Mo $4d^5$ ($g \approx$ 2.006), which increases the g value of Mo^{5+}. The results mentioned above conclusively suggest that the coexistence of molybdate and thiourea in the reactions of BMO/PI not only can promote the further polymerization of dendrite and growth to an ordered 2D multilayer crystal but also can change the electronic charge distribution on the π-conjugated framework of PI through the strong coordination of N atoms to Mo of BMO.

3.2. Optical and Electronic Properties. As shown in Figure 6, after the introduction of BMO, the absorption edge of the PI sample gradually red-shifted and the light absorption in the visible region was obviously enhanced with the increasing concentration of BMO, which agrees well with the color change of BMO/PI samples that vary from bright yellow to dark gray (Figure S5b of the Supporting Information).

It can be estimated from the intercept on the wavelength axis for a tangent line drawn in the UV–vis spectra of the samples, the bandgaps of PI, 3.0BMO/PI, and BMO are 2.79, 2.56, and 2.24 eV, respectively (Figure S8a of the Supporting Information). The trend of the VB edge downshift from 1.0 to 1.35 eV is also evidenced in the VBXPS of PI and 3.0BMO/PI (Figure S8b,c of the Supporting Information). Combining these findings with the UV–vis and VBXPS results, we determined the schematic band structure of PI, 3.0BMO/PI, and BMO (Figure 7). It is more clearly observed from Figure 7

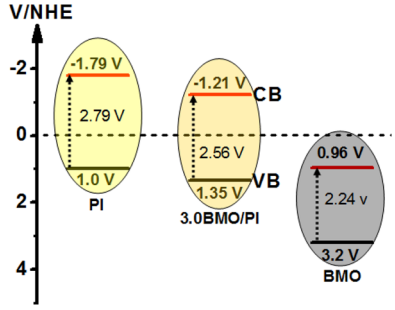

Figure 7. Schematic band structure of PI, 3.0BMO/PI and BMO.

that the bandgap of the 3.0BMO/PI photocatalyst is narrowed from 2.79 to 2.56 V. More importantly, the CB and VB edges of PI downshift after the introduction of BMO, which are very important for simultaneously narrowing the bandgap for absorption of visible light and lowering the energy level of VB for improving the stability of BMO/PI. It is well-known that the oxidation ability of the photoinduced hole and the reduction ability of the photoinduced electron are relevant to the energy level of VB and CB.[45] These results indicate that the incorporation of BMO with a lower CB and VB energy level [3.2 eV (see Figure S8d of the Supporting Information)] on PI indeed effectively lowers the VB level of the resulting BMO/PI composite and thus enhances the photooxidation ability. Remarkably, the fluorescence intensities of the BMO/PI composite samples decrease with the increase in BMO content (Figure 8). This occurrence is attributed to the efficient charge transfer between BMO and PI, thus leading to an improvement in the separation efficiency of the photogenerated electron/hole

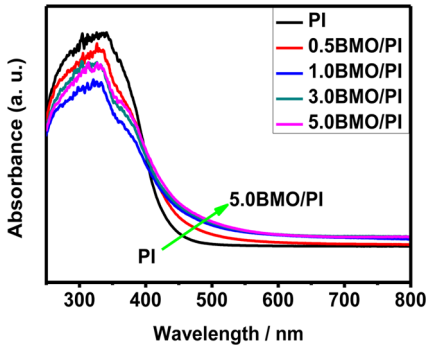

Figure 6. UV–vis absorption spectrum of PI and BMO/PI composite samples.

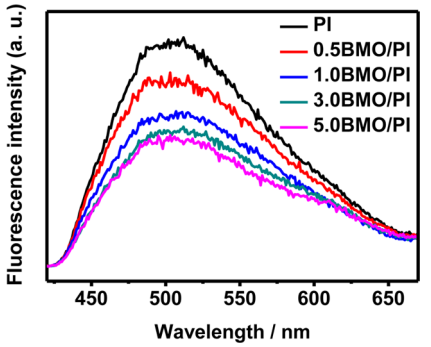

Figure 8. Comparison of photoluminescence (PL) spectra of PI and BMO/PI composite samples.

DOI: 10.1021/acsami.5b01356
ACS Appl. Mater. Interfaces 2015, 7, 14628–14637

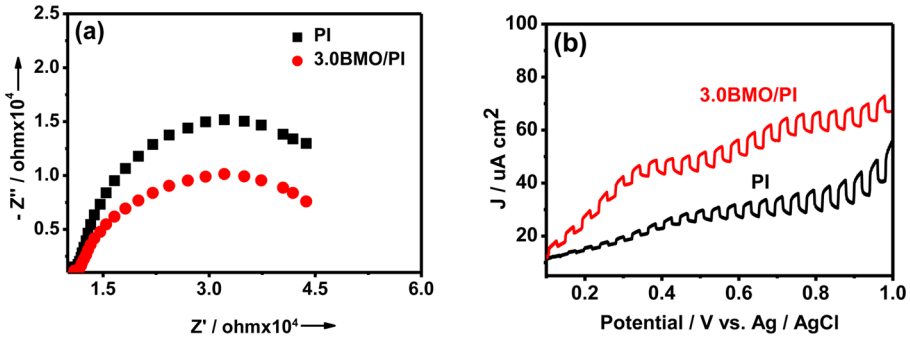

Figure 9. (a) EIS Nyquist plots of electrochemical impedance spectroscopy with PI and the 3.0BMO/PI composite in the dark. (b) Photocurrent–potential curves of PI and the 3.0BMO/PI electrode in the 0.5 mol L^{-1} Na_2SO_4 aqueous solution under visible light irradiation.

pairs, which will facilitate the photocatalytic performance of the BMO/PI.

To gain more information about the transmission properties of the carriers, EIS and photocurrent measurement experiments were conducted (Figure 9). The charge transfer rate in the dark was studied by electrochemical impedance spectroscopy (EIS) (Figure 9a), and the expected semicircular Nyquist plots for PI and 3.0BMO/PI, with an obviously decreased diameter for 3.0BMO/PI, were obtained. Similarly, the photocurrent output of 3.0BMO/PI is much higher than that of PI as shown in Figure 9b.

These results imply that BMO/PI indeed has transfer and separation efficiency of the charge carriers improved compared to those of the PI. These are attributed to the enhanced crystallinity of BMO/PI and Mo^{5+} as an electronic pond in transferring photogenerated electrons to the surface of photocatalyst in a timely fashion.

3.3. Photocatalytic Activity. To verify the analysis mentioned above, the photocatalytic activities of PI, MoO_3, BMO, and BMO/PI composite samples are evaluated by the decomposition of MO in solution (4 mg L^{-1}) and shown in Figure 10. It is found that the photolysis of MO under visible

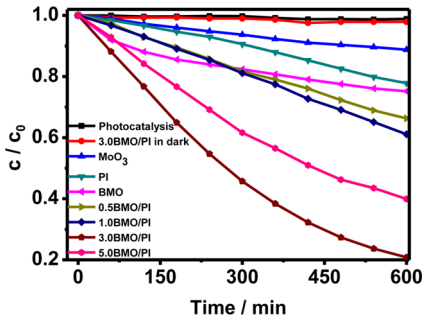

Figure 10. Comparison of the photocatalytic degradation of MO over different catalysts under visible light illumination (λ > 420 nm). The initial point at time zero was used as C_0.

light irradiation is negligible in the absence of photocatalyst, and almost no degradation of MO happens on 3.0BMO/PI in the dark even for 10 h because of the stable structure of MO. Only under the irradiation of a xenon 300 W lamp equipped with a cutoff filter (λ > 420 nm) was different degradation activity for MO obtained on the prepared samples, which indicates that the decomposition of MO on these samples is indeed driven by visible light. To further confirm the direct correlation between the energy of the irradiated light and the activity of the 3.0BMO/PI sample, the wavelength dependence of the rates of MO degradation for 3.0BMO/PI was examined using different band-pass filters (Figure S9a of the Supporting Information). The activity trend matches well with its absorption edge, confirming the MO degradation reaction is indeed driven by the excitation of the photons from the bandgap transition of 3.0BMO/PI. From Figure 10, it can be clearly seen that the photocatalytic activity of BMO is higher than that of MoO_3, which can be ascribed to the extended absorption of visible light of BMO (Figure S9b of the Supporting Information). Notably, all the BMO/PI hybrid composites display improved activities compared with those of pristine PI and BMO, indicating the loaded BMO on PI not only extends the absorption for visible light of PI but also improves the carrier transportation of PI. The degradation activity of BMO/PI increases initially and then reaches a maximum when the BMO content in the composite sample is ~3.0 wt %. The photocatalytic performance of the BMO/PI sample is in accordance with their PL emission at 510 nm, in which the emission intensity gradually decreases when the BMO content increases from 0.5 to 3.0 wt % in BMO/PI samples (Figure 8), mirroring the fact that the separation efficiency of photogenerated electron/hole pairs was improved after BMO had been loaded onto PI and increased with the content of BMO, which will improve the photocatalytic performance of the BMO/PI. However, further adding BMO to a level of 5.0 wt % resulted in a drop in the photocatalytic activity (Figure 10). We know that the photocatalytic activity of a catalyst is affected by many factors, e.g., light absorption, separation efficiency of photogenerated electron/hole pairs, crystallinity of the catalyst, etc. For 5.0BMO/PI, although the separation efficiency of the photogenerated electron/hole pairs is little better than that of 3.0BMO/PI (Figure 8), its light absorption for visible light is not stronger than that of 3.0BMO/PI and especially the lower crystallinity of 5.0BMO/PI (Figure 1) is likely to decrease its photocatalytic activity.

Remarkably, 3.0BMO/PI shows the best performance among the prepared photocatalysts, which is ~4 times higher than that of PI. Although the amount of BMO loaded in PI is small, the corresponding improvement in the photocatalytic performance of PI due to BMO is very significant. As for the drop in the activity of the samples with heavy loadings of BMO, it is likely due to the shading effect that can seriously block the absorption of the incident light by PI. This hypothesis is supported by the UV–vis spectra (Figure 6). In Figure 6, the UV–vis spectra lines of 1.0-, 3.0-, and 5.0BMO/PI samples in the visible light region almost overlap, indicating adding more BMO in PI does not cause an increase in incident light absorption.

DOI: 10.1021/acsami.5b01356
ACS Appl. Mater. Interfaces 2015, 7, 14628–14637

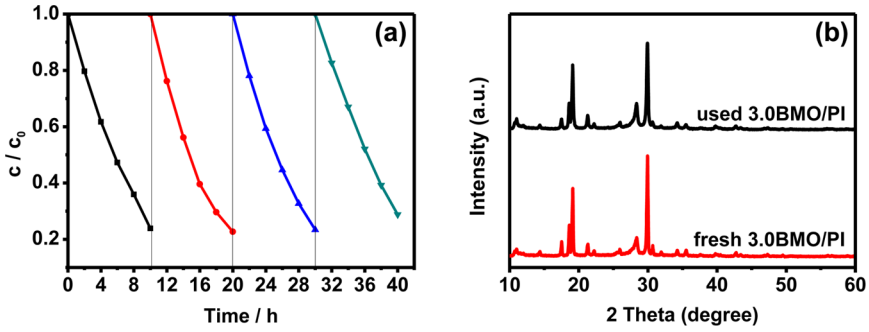

Figure 11. (a) Cycling runs for the photodegradation of MO in the presence of the 3.0BMO/PI composite sample under visible light illumination. (b) XRD patterns of 3.0BMO/PI before and after photodegradation of MO under visible light illumination.

Another important criterion for a good photocatalyst is high durability. To assess the stability of this catalyst, photocatalytic degradation of MO was continuously performed on the 3.0BMO/PI sample for 40 h in four cycles. As shown in Figure 11a, no obvious decrease in the degradation activity of the 3.0BMO/PI sample was observed and its XRD pattern is similar before and after reaction (Figure 11b). These results indicate that the BMO/PI composite has satisfied the stability and recyclability for the degradation of organic pollutants.

To investigate the photocatalytic mechanism of the BMO/PI composite in more detail, some control experiments were conducted by changing the reaction atmosphere or introducing scavengers into the photodegradation system of MO to determine the role of photogenerated electrons or holes, respectively. Generally, the photogenerated electrons work via the reduction of O_2 to form reactive superoxide radical anion ($O_2^{\bullet-}$), and the photogenerated holes react with H_2O to form hydroxyl radicals ($OH^{\bullet}$).[12] Therefore, N_2 purging experiments are first conducted to purge O_2 to determine the effect of photogenerated electrons on MO degradation over BMO/PI. It was observed that the photodegradation rate of MO over 3.0BMO/PI decreases dramatically under N_2, indicating the photogenerated electrons play a crucial role (Figure S10 of the Supporting Information). A further investigation was conducted by using KI as a photogenerated hole (h^+) scavenger to confirm the effect of holes for the photocatalytic activity of BMO/PI because holes can oxide I^- ions into I_2 in the photocatalytic process. As shown in Figure S10 of the Supporting Information, the photodegradation activity of 3.0BMO/PI only slightly decreases after the addition of KI into the photodegradation system of MO, indicating that photogenerated holes are not the main reactive species in the photocatalytic process. Additionally, it is noticed that there are certain amounts of Mo^{4+} in the used 3.0BMO/PI (Figure S11 of the Supporting Information), implying a part of the Mo^{5+} was reduced to Mo^{4+} by photogenerated electrons during the photocatalytic reaction. Therefore, a possible photocatalytic mechanism of the BMO/PI composite can be described as follows (steps 1−7). Under visible light irradiation, photogenerated electrons (e^-) transfer from PI to BMO, leaving a photogenerated hole (h^+) on the VB of PI. The O_2 absorbed on the surface of BMO can efficiently capture the e^- to form predominant active $O_2^{\bullet-}$ species. The h^+ reacts with H_2O and forms $OH^{\bullet}$. Then reactive radicals $OH^{\bullet}$ and $O_2^{\bullet-}$ oxidize MO into inorganic small molecules, such as H_2O, CO_2, etc., to degrade the pollutant. Meanwhile, small parts of Mo^{5+} ions probably are reduced to Mo^{4+} by accepting photogenerated electrons, while these Mo^{4+} ions can be reoxidized into Mo^{5+} by the absorbed O_2 on the surface of BMO/PI samples; the latter step accompanies the release of $O_2^{\bullet-}$ species and keeps the balance of Mo species in different valence states during the photocatalytic process.

To improve our understanding of the mechanism of the photocatalytic degradation of organic pollutants, we draw a simple diagram as shown in Figure 12. Under visible light

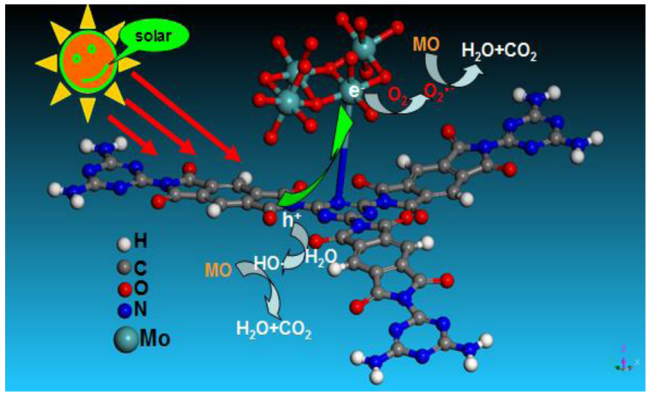

Figure 12. Schematic of the photogenerated charge carrier's separation and transfer in the BMO/PI system under visible light irradiation.

irradiation, the photogenerated electron (e^-) transfers from PI to BMO, leaving the photogenerated hole (h^+) on the PI. The O_2 absorbed on the surface of BMO can efficiently capture the e^- to form active $O_2^{\bullet-}$ species.[46] The photogenerated hole h^+ reacts with H_2O and forms $OH^{\bullet}$. Then active radicals $O_2^{\bullet-}$ and $OH^{\bullet}$ oxidize MO into small inorganic molecules, such as H_2O, CO_2, etc.[12] Therefore, the efficient photocatalytic decolorization of MO can smoothly proceed.

$$PI + h\nu \rightarrow h^+ + e^- \quad (1)$$

$$e^- + O_2 \rightarrow O_2^{\bullet-} \quad (2)$$

$$h^+ + H_2O \rightarrow OH^{\bullet} \quad (3)$$

$$O_2^{\bullet-} + MO \rightarrow CO_2 + H_2O + e^- \quad (4)$$

$$OH^{\bullet} + MO \rightarrow CO_2 + H_2O \quad (5)$$

$$e^- + Mo^{5+} \rightarrow Mo^{4+} \quad (6)$$

$$Mo^{4+} + O_2 \rightarrow Mo^{5+} + O_2^{\bullet-} \quad (7)$$

DOI: 10.1021/acsami.5b01356
ACS Appl. Mater. Interfaces 2015, 7, 14628−14637

4. CONCLUSIONS

In summary, we adopt a one-pot solid thermal copolymerization approach to successfully synthesize a novel hybrid polymer photocatalyst BMO/PI. The decomposition of coexisting thiourea in the reactants results in a hypoxia reaction condition, which leads to the formation of oxygen vacancies and thus black MoO_3 (BMO) on PI. The incorporation of BMO onto PI not only extends the absorption range of PI for visible light but also enhances the separation efficiency of the photogenerated electron/hole pairs through the Mo−N coordination bond, thus leading to an enhanced activity and durability in degradation of MO under visible light irradiation.

■ ASSOCIATED CONTENT

Supporting Information

Powder XRD patterns of 3.0BMO/PI, 3.0S/PI, 3.0MoO_3/PI, PI, BMO, and MoO_3; TEM images of PI, BMO, and MoO_3; SEM image of PI; EDS analysis of 3.0BMO/PI; colors of MoO_3, BMO, PI, and BMO/PI samples; EPR spectra of MoO_3 and BMO; XPS spectra of MoO_3, BMO, PI, 3.0MoO_3/PI, and used 3.0BMO/PI; VBXPS spectra of PI, 3.0BMO/PI, and BMO; UV−vis absorption spectra of PI, 3.0BMO/PI, BMO, and MoO_3; dependence of degradation activity on wavelength by 3.0BMO/PI; and effects of KI and purging N_2 as h^+ and $O_2^{\bullet-}$ scavengers on the degradation of MO in the presence of 3.0BMO/PI under visible light irradiation. The Supporting Information is available free of charge on the ACS Publications website at DOI: 10.1021/acsami.5b01356.

■ AUTHOR INFORMATION

Corresponding Authors

*E-mail: wangy@nju.edu.cn.
*E-mail: zgzou@nju.edu.cn.

Notes

The authors declare no competing financial interest.

■ ACKNOWLEDGMENTS

This work was financially supported by NSFC (21273111, 21273106, and 51272101), the National Basic Research Program of China (973 Program, 2013CB632404), and the Jiangsu Provincial Natural Science Foundation (BK20130053). We thank Analysis Center of Nanjing University for sample characterization.

■ REFERENCES

(1) Murugan, K.; Rao, Tata N.; Gandhi, Ashutosh S.; Murty, B. S. Effect of Aggregation of Methyleneblue Dye on TiO_2 Surface in Self-Cleaning Studies. *Catal. Commun.* **2010**, *11*, 518−521.
(2) Jiang, T. F.; Xie, T. F.; Chen, L. P.; Fu, Z. W.; Wang, D. J. Carrier. Concentration-Dependent Electron Transfer in Cu_2O/ZnO Nanorod Arrays and Their Photocatalytic Performance. *Nanoscale* **2013**, *5*, 2938−2944.
(3) Lin, Y. J.; Yuan, G. B.; Sheehan, S.; Zhou, S.; Wang, D. W. Hematite-Based Solar Water Splitting: Challenges and Opportunities. *Energy Environ. Sci.* **2011**, *4*, 4862−4869.
(4) Wang, X. C.; Maeda, K.; Thomas, A.; Takanabe, K.; Xin, G.; Carlsson, J. M.; Domen, K.; Antonietti, M. A Metal-Free Polymeric Photocatalyst for Hydrogen Production from Water under Visible Light. *Nat. Mater.* **2009**, *8*, 76−80.
(5) Zhang, J. S.; Chen, X. F.; Takanabe, K.; Maeda, K.; Domen, K.; Epping, J. D.; Fu, X. Z.; Antonietti, M.; Wang, X. C. Synthesis of a Carbon Nitride Structure for Visible-Light Catalysis by Copolymerization. *Angew. Chem., Int. Ed.* **2010**, *49*, 441−444.
(6) Stegbauer, L.; Schwinghammer, K.; Lotsch, B. V. A Hydrazone-Based Covalent Organic Framework for Photocatalytic Hydrogen Production. *Chem. Sci.* **2014**, *5*, 2789−2793.
(7) Schwab, M. G.; Hamburger, M.; Feng, X.; Shu, J.; Spiess, H. W.; Wang, X.; Antonietti, M.; Mullen, K. Photocatalytic Hydrogen Evolution through Fully Conjugated Poly(Azomethine) Networks. *Chem. Commun.* **2010**, *46*, 8932−8934.
(8) Wan, S.; Gandara, F.; Asano, A.; Furukawa, H.; Saeki, A.; Dey, S. K.; Liao, L.; Ambrogio, M. W.; Botros, Y. Y.; Duan, X. F.; Seki, S.; Stoddart, J. F.; Yaghi, O. M. Covalent Organic Frameworks with High Charge Carrier Mobility. *Chem. Mater.* **2011**, *23*, 4094−4097.
(9) Hou, Y. D.; Laursen, A. B.; Zhang, J. S.; Zhang, G. G.; Zhu, Y. S.; Wang, X. C.; Dahl, S.; Chorkendorff, I. Layered Nanojunctions for Hydrogen-Evolution Catalysis. *Angew. Chem.* **2013**, *125*, 3709−3713.
(10) Xiang, Q. J.; Yu, J. G.; Jaroniec, M. Preparation and Enhanced Visible-Light Photocatalytic H_2-Production Activity of Graphene/C_3N_4 Composites. *J. Phys. Chem. C* **2011**, *115*, 7355−7363.
(11) Yun, J. M.; Noh, Y. J.; Yeo, J. S.; Go, Y. J.; Na, S. I.; Jeong, H. G.; Kim, J. W.; Lee, S.; Kim, S. S.; Koo, H. Y.; Kim, T. W.; Kim, D. Y. Efficient Work-Function Engineering of Solution Processed MoS_2 Thin-Films for Novel Hole and Electron Transport Layers Leading to High Performance Polymer Solar Cells. *J. Mater. Chem. C* **2013**, *1*, 3777−3783.
(12) Zhou, X. S.; Jin, B.; Chen, R. Q.; Peng, F.; Fang, Y. P. Synthesis of Porous Fe_3O_4/g-C_3N_4 Nanospheres as Highly Efficient and Recyclable Photocatalysts. *Mater. Res. Bull.* **2013**, *48*, 1447−1452.
(13) Park, S. J.; Li, K.; Jin, F. L. Synthesis and Characterization of Hyper-Branched Polyimides. *Mater. Chem. Phys.* **2008**, *108*, 214−219.
(14) Jin, Y. X.; Tang, J.; Hu, J.; Han, X.; Shang, Y. Z.; Liu, H. L. One-Step Fabrication of Ultralow Dielectric Polyimide Films Consisting of Size-Controlled Mesoporous Nanoparticles. *Colloids Surf., A* **2011**, *392*, 178−186.
(15) Ekinci, E.; Emre, F. B.; Köytepe, S.; Seçkin, T. Preparation, Characterization and H_2O_2 Selectivity of Hyperbranched Polyimides Containing Triazine. *J. Polym. Res.* **2005**, *12*, 205−210.
(16) Kuhn, P.; Krüger, K.; Thomas, A.; Antonietti, M. "Everything is Surface": Tunable Polymer Organic Frameworks with Ultrahigh Dye Sorption Capacity. *Chem. Commun.* **2008**, 5815−5817.
(17) Guo, Y.; Chu, S.; Yan, S. C.; Wang, Y.; Zou, Z. G. Developing a Polymeric Semiconductor Photocatalyst with Visible Light Response. *Chem. Commun.* **2010**, *46*, 7325−7327.
(18) Chu, S.; Wang, Y.; Guo, Y.; Zhou, P.; Yu, H.; Luo, L. L.; Kong, F.; Zou, Z. G. Facile Green Synthesis of Crystalline Polyimide Photocatalyst for Hydrogen Generation from Water. *J. Mater. Chem.* **2012**, *22*, 15519−15521.
(19) Greiner, M. T.; Chai, L.; Helander, M. G.; Tang, W. M.; Lu, Z. H. Transition Metal Oxide Work Functions: The Influence of Cation Oxidation State and Oxygen Vacancies. *Adv. Funct. Mater.* **2012**, *22*, 4557−4568.
(20) Kröger, M.; Hamwi, S.; Meyer, J.; Riedl, T.; Kowalsky, W.; Kahn, A. P-Type Doping of Organic Wide Band Gap Materials by Transition Metal Oxides: A Case-Study on Molybdenum Trioxide. *Org. Electron.* **2009**, *10*, 932−938.
(21) Hamwi, S.; Meyer, J.; Kröger, M.; Winkler, T.; Witte, M.; Riedl, T.; Kahn, A.; Kowalsky, W. The Role of Transition Metal Oxides in Charge-Generation Layers for Stacked Organic Light-Emitting Diodes. *Adv. Funct. Mater.* **2010**, *20*, 1762−1766.
(22) Cheung, C. H.; Song, W. J.; So, S. K. Role of Air Exposure in The Improvement of Injection Efficiency of Transition Metal Oxide/Organic Contact. *Org. Electron.* **2010**, *11*, 89−94.
(23) Meyer, J.; Hamwi, S.; Kröger, M.; Kowalsky, W.; Riedl, T.; Kahn, A. Transition Metal Oxides for Organic Electronics: Energetics, Device Physics and Applications. *Adv. Mater.* **2012**, *24*, 5408−5427.
(24) Yang, J. P.; Xiao, Y.; Deng, Y. H.; Duhm, S.; Ueno, N.; Lee, S. T.; Li, Y. Q.; Tang, J. X. Electric-Field-Assisted Charge Generation and Separation Process in Transition Metal Oxide-Based Interconnectors for Tandem Organic Light-Emitting Diodes. *Adv. Funct. Mater.* **2012**, *22*, 600−608.

DOI: 10.1021/acsami.5b01356
ACS Appl. Mater. Interfaces 2015, 7, 14628−14637

(25) Wang, X. C.; Chen, X. F.; Thomas, A.; Fu, X. Z.; Antonietti, M. Metal-Containing Carbon Nitride Compounds: A New Functional Organic-Metal Hybrid Material. *Adv. Mater.* **2009**, *21*, 1609−1612.
(26) Wang, C. C.; Guo, Y.; Yang, Y.; Chu, S.; Zhou, C. K.; Wang, Y.; Zou, Z. G. Sulfur-Doped Polyimide Photocatalyst with Enhanced Photocatalytic Activity under Visible Light Irradiation. *ACS Appl. Mater. Interfaces* **2014**, *6*, 4321−4328.
(27) Spitler, E. L.; Dichtel, W. R. Lewis Acid-Catalysed Formation of Two-Dimensional Phthalocyanine Covalent Organic Frameworks. *Nat. Chem.* **2010**, *2*, 672−677.
(28) Bojdys, M. J.; Wohlgemuth, S. A.; Thomas, A.; Antonietti, M. Ionothermal Route to Layered Two-Dimensional Polymer-Frameworks Based on Heptazine Linkers. *Macromolecules* **2010**, *43*, 6639−6645.
(29) Song, L. X.; Xia, J.; Dang, Z.; Yang, J.; Wang, L. B.; Chen, J. Formation, Structure and Physical Properties of a Series of Alpha-MoO_3 Nanocrystals: Nrom 3D to 1D and 2D. *CrystEngComm* **2012**, *14*, 2675−2682.
(30) Sasidharan, M.; Gunawardhana, N.; Noma, H.; Yoshio, M.; Nakashima, K. Alpha-MoO_3 Hollow Nanospheres as an Anode Material for Li-Ion Batteries. *Bull. Chem. Soc. Jpn.* **2012**, *85*, 642−646.
(31) Ng, T. W.; Yang, Q. D.; Mo, H. W.; Lo, M. F.; Zhang, W. J.; Lee, C. S. Wide-Spectral Photoresponse of Black Molybdenum Oxide Photodetector via Sub-Bandgap Electronic Transition. *Adv. Opt. Mater.* **2013**, *1*, 699−702.
(32) Zhang, J. Y.; Wang, J. J.; Zhao, Z. Y.; Yu, T.; Feng, J. Y.; Yuan, Y. J.; Tang, Z. K.; Liu, Y. H.; Li, Z. S.; Zou, Z. G. Reconstruction of The (001) Surface of TiO_2 Nanosheets Induced by The Fluorine-Surfactant Removal Process under UV-Irradiation for Dye-Sensitized Solar Cells. *Phys. Chem. Chem. Phys.* **2012**, *14*, 4763−4769.
(33) Ryadun, A. A.; Nadolinny, V. A.; Pavlyuk, A. A.; Trifonov, V. A. Influence of Photoexcitation on The EPR Spectra of Mo^{5+} in $Li_2Zn_2(MoO_4)_3$: Ce^{3+},Cu^{2+} Crystals Annealed in a CO_2 Atmosphere. *Phys. Solid State* **2013**, *55*, 720−724.
(34) Tokarz-Sobieraj, R.; Hermann, K.; Witko, M.; Blume, A.; Mestl, G.; Schlögl, R. Properties of Oxygen Sites at The MoO_3(010) Surface: Density Functional Theory Cluster Studies and Photoemission Experiments. *Surf. Sci.* **2001**, *489*, 107−125.
(35) Chu, S.; Wang, Y.; Wang, C. C.; Yang, J. C.; Zou, Z. G. Bandgap Modulation of Polyimide Photocatalyst for Optimum H_2 Production Activity under Visible Light Irradiation. *Int. J. Hydrogen Energy* **2013**, *38*, 10768−10772.
(36) Hermann, K.; Witko, M.; Michalak, A. Density Functional Studies of The Electronic Structure and Adsorption at Molybdenum Oxide Surfaces. *Catal. Today* **1999**, *50*, 567−577.
(37) Zeng, S. Z.; Guo, L. M.; Cui, F. M.; Gao, Z.; Zhou, J.; Shi, J. L. In Situ Self-Assembly of Zigzag Polyimide Chains to Crystalline Branched Supramolecular Structures with High Surface Area. *Macromol. Chem. Phys.* **2010**, *211*, 698−705.
(38) Chu, S.; Wang, Y.; Guo, Y.; Feng, J. Y.; Wang, C. C.; Luo, W. J.; Fan, X. X.; Zou, Z. G. Band Structure Engineering of Carbon Nitride: In Search of a Polymer Photocatalyst with High Photooxidation Property. *ACS Catal.* **2013**, *3*, 912−919.
(39) Wang, X. L.; Li, J.; Tian, A. X.; Liu, G. C.; Gao, Q.; Lin, H. Y.; Zhao, D. A. 3D Organopolymolybdate Polymer with Unusual Topology Functionalized by 1,4-Bis(1,2,4-triazol-1-yl)Butane Through Mo-N Bond. *CrystEngComm* **2011**, *13*, 2194−2196.
(40) Spevack, P. A.; McIntyre, N. S. A Raman and XPS Investigation of Supported Molybdenum Oxide thin Films. 1. Calcinations and Reduction studies. *J. Phys. Chem.* **1993**, *97*, 11020−11030.
(41) Ng, T. W.; Lo, M. F.; Yang, Q. D.; Fung, M. K.; Lee, C. S. Near-Infrared Electric Power Generation Through Sub-Energy-Gap Absorption in an Organic−Inorganic Composite. *Adv. Funct. Mater.* **2012**, *22*, 3035−3042.
(42) He, Y. M.; Zhang, L. H.; Wang, X. X.; Wu, Y.; Lin, H. J.; Zhao, L. H.; Weng, W. Z.; Wan, H. L.; Fan, M. H. Enhanced Photodegradation Activity of Methyl Orange over Z-Scheme type MoO_3-g-C_3N_4 Composite under Visible Light Irradiation. *RSC Adv.* **2014**, *4*, 13610−63619.
(43) Zhang, J. S.; Zhang, G. G.; Chen, X. F.; Lin, S.; Möhlmann, L.; Dołęga, G.; Lipner, G.; Antonietti, M.; Blechert, S.; Wang, X. C. Co-Monomer Control of Carbon Nitride Semiconductors to Optimize Hydrogen Evolution with Visible Light. *Angew. Chem., Int. Ed.* **2012**, *51*, 3183−3187.
(44) Radha, K. C.; Anavekar, R. V.; Rao, J. L.; Chakradhar, R. P. S. EPR and Optical Studies of Mo^{5+} Ions in Lithium Molybdoborate Glasses. *Appl. Magn. Reson.* **2008**, *35*, 1−13.
(45) Linsebigler, A. L.; Lu, G.; Yates, J. T. Photocatalysis on TiO_2 Surfaces: Principles, Mechanisms, and Selected Results. *Chem. Rev.* **1995**, *95*, 735−758.
(46) Yang, D. J.; Liu, H. W.; Zheng, Z. F.; Yuan, Y.; Zhao, J. C.; Waclawik, E. R.; Ke, X. B.; Zhu, H. Y. An Efficient Photocatalyst Structure: TiO_2 (B) Nanofibers with a Shell of Anatase Nanocrystals. *J. Am. Chem. Soc.* **2009**, *131*, 17885−17893.

DOI: 10.1021/acsami.5b01356
ACS Appl. Mater. Interfaces 2015, 7, 14628−14637